


M. MEYER  
O.F. SCHIRMER   
R. PANKRATH

# Performance of photorefractive crystals as derived from EPR-based defect studies: application to BaTiO<sub>3</sub>:Rh and Ba<sub>0.77</sub>Ca<sub>0.23</sub>TiO<sub>3</sub>:Rh

Fachbereich Physik, Universität Osnabrück, 49069 Osnabrück, Germany

Received: 11 February 2004/Revised version: 6 May 2004  
Published online: 20 July 2004 • © Springer-Verlag 2004

**ABSTRACT** A method is introduced which allows us to predict the performance of a photorefractive material quantitatively using electron paramagnetic resonance (EPR)-based defect studies. This includes the determination of the defect densities and the parameters governing their light-induced charge changes. On this basis the effective trap densities and the photorefractive response times are calculated. All quantities can be determined without theoretical simplifications such as employed in previous approaches to the problem. The method is applied to BaTiO<sub>3</sub> and congruently melting Ba<sub>0.77</sub>Ca<sub>0.23</sub>TiO<sub>3</sub>, both doped with rhodium. The iron defects, present as background contaminations, are fully taken into account. Their influence on the intensity saturating the space charges is calculated on this basis. The complete energy dependences of the absorption cross sections of all optically active Rh and Fe defects are given.

PACS 42.70.Nq; 76.30.Mi; 78.40.-q

## 1 Introduction

The strength of the light-induced space-charge fields,  $E_{sc}$ , is the central quantity determining the photorefractive performance of materials showing a linear electrooptic effect. These fields are caused by the photoionization of defects under inhomogeneous illumination and by the subsequent transport of the liberated charge carriers towards the darker regions of the crystal, where they are trapped by the existing lattice perturbations. In the absence of an external electric field, diffusion is the predominant transport mechanism active in BaTiO<sub>3</sub> and Ba<sub>1-x</sub>Ca<sub>x</sub>TiO<sub>3</sub> [1, 2]. The space-charge fields are related to the effective trap density  $N_{eff}$ , a quantity depending on the charge states of the defects and their concentrations; see below. In order to predict the performance of a material it is thus necessary to determine these quantities.

In the most straightforward way this can be performed by electron paramagnetic resonance (EPR) investigations of the relevant materials, yielding information on these defect items: charge and density. This, however, refers to an ideal situation. Not all defects are EPR-active, even if they happen to be paramagnetic. The problem can be circumvented if emphasis is

first laid on the optical absorption of the defects, usually available irrespective of whether the defects are EPR-active or EPR-silent. If the corresponding absorption bands and their intensities can be assigned to the responsible defects, their charge states, and their concentrations, all necessary information is available to infer  $N_{eff}$ . The route towards this goal starts with the simultaneous registration of the changes of the EPR as well as of the optical signals of all defects in a specimen induced by homogeneous illumination. The latter phenomenon is based on the photochromicity usually exhibited by inorganic photorefractive materials – if not at room temperature then at low ones. The common and consistent interpretation of both types of signal changes leads to the wanted information: charge and density of the EPR-silent defects also. Examples will be given below.

By studying the time dependences of the defect concentrations after the illuminating light is switched on or off, the parameters describing the temporal response of the related charge-transfer processes can additionally be obtained. This will allow us to determine the parameters governing the transfer events and, from them, the photorefractive response times.

The method will be applied to the photorefractive materials BaTiO<sub>3</sub> (BT) and Ba<sub>0.77</sub>Ca<sub>0.23</sub>TiO<sub>3</sub> (BCT), doped with rhodium (Rh), known to improve the photorefractive sensitivity of the materials in the near infrared [2–7]. BCT, in principle, is a useful replacement of BT in this context, avoiding the drawbacks of the latter connected with its cubic to tetragonal phase transition near 8 °C [8, 9]. The indicated composition of BCT refers to its congruently melting composition. Some general properties of both materials are listed in Table 1. Extending a similar previous study of the photorefractive performance of BT:Rh [10], we now quantitatively include not only the Rh impurities but also the subsystem of Fe background defects usually contained in such crystals [11]. Based on the experience gathered with BT:Rh we shall extend the investigation to BCT:Rh, where the so far unavoidable Fe contamination is assumed to be still more important [7].

Huot et al. [12] and Corner et al. [13] were the first to study the photorefractive performance of the system BT:Rh by investigating the consequences of the three-valence model [14] constituted by the three charge states Rh<sup>3+</sup>, Rh<sup>4+</sup>, and Rh<sup>5+</sup> occurring in as-grown or oxidized crystals [10, 15]. Using experimentally determined values of light-induced absorption and beam-coupling gains at 1.06 μm, the authors derived

		BT [50]	BCT
density (tetragonal phase)	$\rho$ (g/cm <sup>3</sup> )	6.02	5.58 [8]
lattice parameter (tetragonal phase)	$a$ (nm)	0.3992	0.3962 [8]
	$c$ (nm)	0.4036	0.3999 [8]
band gap energy	$E_g$ (eV)	$\sim 3.1$	$\sim 3.2$ [9]
refractive index (ordinary polarized light)	$n_o$ ( $\lambda = 800$ nm)	2.37 [51]	2.36 [52]
	$n_o$ ( $\lambda = 632$ nm)	2.41 [51]	2.40 [52]
	$n_o$ ( $\lambda = 400$ nm)	2.71 [51]	2.68 [52]
dielectric constant $\epsilon_r$	$\epsilon_{11}$	4300 [53]	120 [8]
	$\epsilon_{33}$	168 [53]	240 [8]
transition temperature (tetragonal–cubic)	$T_c$ (K)	$\sim 403$	$\sim 371$ [8]
(orthorhombic–tetragonal)	$T_c$ (K)	$\sim 281$	$< 30$ [54]

**TABLE 1** Comparison of some BT and BCT crystal data. Where not stated differently, the data refer to room temperature

the parameters governing the charge-transfer processes. Bernhardt et al. [7, 16] transferred this analysis to the operation of BCT:Rh at 850 nm. They also took into account the presence of Fe as a background contamination by considering the charge states  $\text{Fe}^{3+}$  and  $\text{Fe}^{4+}$ , neglecting the presence of  $\text{Fe}^{5+}$ . Since in these approaches the available experimental information was limited, the authors furthermore had to use a simplified theoretical basis to determine some of the wanted parameters. With a similar approach, Radoua et al. studied the photorefractive performance of BCT:Rh at 1.06  $\mu\text{m}$  [17]. Veber et al. [10] recently introduced EPR to obtain more complete experimental knowledge on BT:Rh and derived the defect densities and the charge-transfer parameters using the full theoretical basis. However, in that paper the influence of Fe was only estimated. This drawback is removed in the present approach; we arrive at the most detailed experimental results and interpret them with the full theory.

The procedure exploited in this paper has grown from previous studies which were focussed on the qualitative clarification of the question of between which defects charge transfers occur in a series of photorefractive crystals [18–22] under illumination. Based on the photochromicity of the materials, EPR studies allowed us to establish the identity and charge states of the defects involved. The present work extends these investigations to the quantitative aspects of light-induced transfers in crystals.

The paper is organized in the following way: after giving some information about the experimental basis of the investigation, in Sect. 2 the knowledge about the EPR-active defects in BT:Rh is summarized. Then it is described how information about the EPR-silent defects is acquired. From the collected data quantities are deduced which can be compared with experimental results, such as  $N_{\text{eff}}$ . In Sect. 3 a similar procedure is applied to obtain and assess the corresponding data for BCT:Rh. Some further experimental questions, concerning both BT:Rh and BCT:Rh, are treated in Sect. 4. A discussion of the general aspects, the merits and the outlook of the method used follows in Sect. 5. Also the parameters derived on this basis, as well as special features of BCT:Rh are treated in this section.

sample (crystal label)	doped with	doping (ppm in melt)	size [mm <sup>3</sup> ]	comment, treatment
BT ('ob 1')	Rh	?	$0.7 \times 4.0 \times 3.0$	as grown <sup>+</sup>
(X17)	Rh	1000	$0.9 \times 3.5 \times 3.3$	as grown
(X70)	Rh	10 000	$0.5 \times 4.0 \times 3.8$	as grown
(X70ox)	Rh	10 000	$0.5 \times 4.0 \times 3.8$	oxidized 2 h, 800 °C, 20 bar in O <sub>2</sub>
(X70red1)	Rh	10 000	$0.5 \times 3.8 \times 3.3$	reduced 2 h, 800 °C, 10 <sup>-3</sup> mbar
(X70red2)	Rh	10 000	$0.5 \times 3.8 \times 3.3$	reduced 2 h, 400 °C, 10 <sup>-3</sup> mbar
(GR120)	Fe	750	$1.0 \times 4.0 \times 2.9$	as grown <sup>+</sup>
(GR87)	Fe	50	$1.2 \times 3.7 \times 2.8$	as grown

<sup>+</sup> chemical analysis available

**TABLE 2** List of BT samples and their treatments

## 2 BaTiO<sub>3</sub>:Rh

### 2.1 Experimental details

Table 2 gives a general overview of the studied BT specimens. Those listed in Table 3, column 1, were investigated in most detail with the present method. Column 2 shows the doping concentrations in the melts, where known. These crystals were kindly made available by H. Hesse, M. Kaczmarek, and D. Rytz. Three of the specimens contain Rh; two are doped only with Fe. EPR measurements were performed with a Bruker 200 D spectrometer, operating near 9.8 GHz. Temperatures below room temperature were achieved with an Oxford Instruments helium-flow cryostat. A two-beam optical spectrometer served to register optical absorption spectra at room temperature. Light-induced absorption changes were recorded with a special setup [23] facilitating simultaneous measurements of the accompanying EPR signal changes, also at low temperatures. This apparatus allows the illumination with pump light – monochromatic and intense – followed by application of probing light – weak and wideband. For details see below. Care was taken to avoid measurement-induced changes of the absorption status of the crystals by keeping the probe light as weak as possible. Photorefractive data of the investigated crystals has been reported before [10, 16]. The specimens were oxidized under 20 bar of pure oxygen at 800 °C for 2 h, whereas reduction was typically performed in a vacuum of 10<sup>-3</sup> mbar, also at 800 °C for 2 h, where not stated differently. A poling of the specimens after the mentioned heat treatments is not necessary, since the EPR and optical investigations, on which our investigations are based, do not require monodomain crystals.

### 2.2 Assignment of the defect optical absorption bands

In as-grown and oxidized BT:Rh crystals, EPR identifies the charge state  $\text{Rh}^{4+}$  [15, 24] and, resulting from the Fe background contamination,  $\text{Fe}^{3+}$  and  $\text{Fe}^{5+}$  [10, 24]. These EPR-active valencies are complemented by the EPR-silent ones  $\text{Rh}^{5+}$ ,  $\text{Rh}^{3+}$ , and  $\text{Fe}^{4+}$  [10]. Their presence is proved, as will be discussed in the following, by a plot showing how the photochromicity depends on the pump energy, such as Fig. 1a. Here the colors indicate the absorption

1	2	3	4	5	6	7	8	9	10	11	12	13
sample (label)	doping (ppm)	method	Fe <sup>3+</sup> (ppm)	Fe <sup>4+</sup> (ppm)	Fe <sup>5+</sup> (ppm)	Fe <sup>tot</sup> (ppm)	Rh <sup>3+</sup> (ppm)	Rh <sup>4+</sup> (ppm)	Rh <sup>5+</sup> (ppm)	Fe <sup>tot</sup> (ppm)	$N_{\text{eff}}$ (pred.) $10^{17} \text{ cm}^{-3}$	$N_{\text{eff}}$ (meas.) $10^{17} \text{ cm}^{-3}$
BT : Rh (‘ob 1’)	?	optical EPR		< 1.0	< 1.0	< 10 [31]	15.5	4.0	1.5	14 [31]	$1.4 \pm 0.8$	0.9 [10]
(X17)	1000	optical EPR	5.0	< 1.0	< 1.0		17.5	8.0	1.5		$1.7 \pm 1.2$	1.7 [16]
(X70)	10000	optical EPR	10.0	< 1.0	< 1.0		60.0	8.0	5.0		$4.8 \pm 2.8$	
(X70ox)	10000	optical EPR	~ 30.0	4.0	2.0		53.0	~ 40.0	6.0		$4.9 \pm 2.9$	
BT : Fe (GR120)	750	optical EPR		10.0	6.0	380 [32,33]					$3.0 \pm 1.8$	
(GR87)	50	optical EPR	360.0	< 1.0	~ 5.0						< 0.4	0.1 [55]
			40.0	< 1.0	< 1.0							

**TABLE 3** Concentrations of the Rh and Fe charge states in the investigated BT:Rh and BT:Fe crystals and the determined  $N_{\text{eff}}$ . The table lists the experimentally determined Fe defect concentrations (columns 4–6), determined by the indicated methods (column 3). For comparison, the chemically determined total Fe concentrations are listed in column 7, where available. Columns 8–11 list the corresponding Rh data. In columns 12 and 13 the  $N_{\text{eff}}$  predicted on the basis of the measured defect concentrations are compared with those measured experimentally, where available

changes, as calibrated by the bar above the figure. The abscissa is the probe-light energy,  $E_{\text{probe}}$ , and the ordinate the pump-light energy,  $E_{\text{pump}}$ . Such a plot results from monitoring the sequence of absorption spectra induced by a succession of pump energies, indicated by the numbered horizontal lines at the left. Illumination starts at the lowest pump energy, number 1, and proceeds according to the rising numbers. After each illumination, lasting 1 min and leading to saturation of the defect charge changes at room temperature, the status of the light-induced absorption is monitored by weak white probe light during about 20 ms. Numerical interpolation between

the discrete absorption spectra leads to the continuous ‘landscape’ shown by Fig. 1a.

Valleys (colors tending towards blue) indicate light-induced transparency, hills (colors towards red) light-induced absorption. The initial, primary charge transfer processes, each resulting from the absorption of a pump-light quantum and thus triggering the light-induced recharging of defects, are characterized by more ‘blue’ transparency features along the diagonal,  $E_{\text{probe}} = E_{\text{pump}}$  [10]. The subsequent processes, following the primary ones, usually lead to structures outside of this diagonal. By studying the changes of the EPR signals

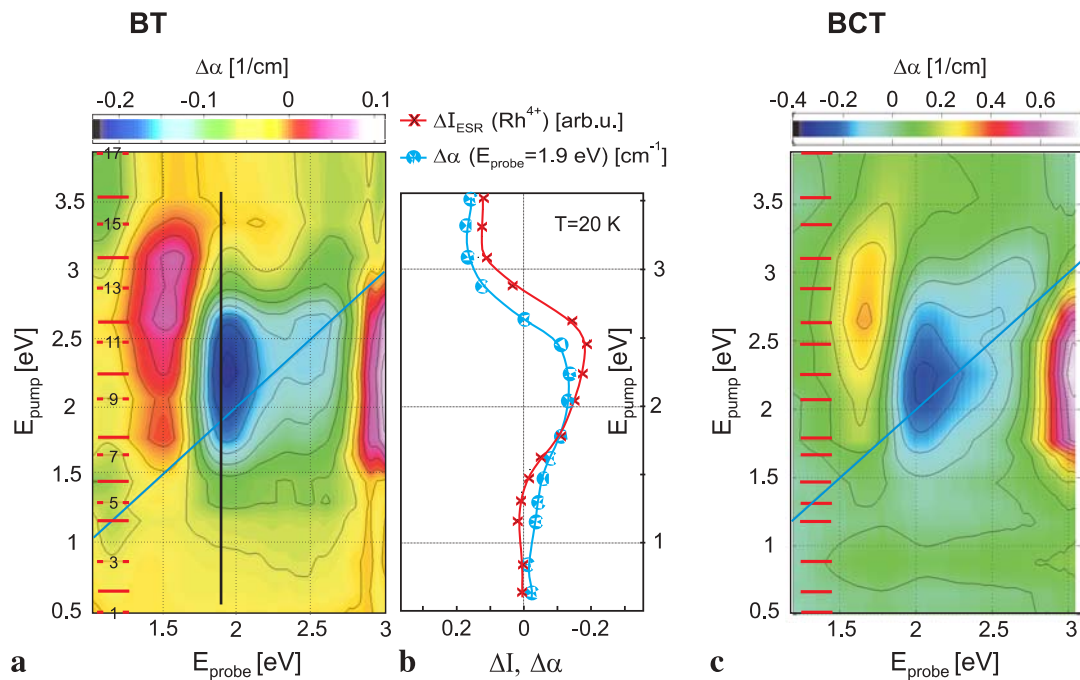


**FIGURE 1** Pump-energy dependence of the photochromicity of BT:Rh (a) and BCT:Rh (c) at room temperature, as plotted in a color code over the field of  $E_{\text{pump}}$  (vertical) and  $E_{\text{probe}}$  (horizontal). The colors are calibrated by the bar at the top. The sequence of pump energies, inducing the absorption changes, are shown as horizontal lines at the left. The numbers indicate the order of their application. In (b) the absorption changes for  $E_{\text{probe}} = 1.9$  eV (vertical line in (a)) are compared to the changes of the EPR signals of Rh<sup>4+</sup>, measured simultaneously. The continuous plots in (a) and (c) result from interpolation between the corresponding discrete absorption spectra

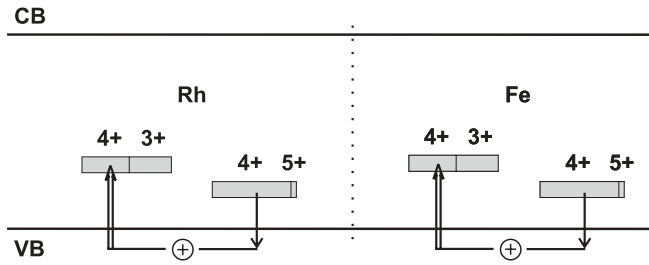


**FIGURE 2** Three-valence models representing the pump-light-triggered recharging among the three charge states of Rh (*left*) and Fe (*right*). Exchange of the holes between both systems is also possible. The *double arrows* indicate the (*primary*) processes resulting from absorption of the pump quantum, the *single arrow* the (*secondary*) follow-up recombination process

simultaneously with those of the optical ones, i.e. under the same pump-light variations, correlations between both phenomena are established. It turns out (Fig. 1b) in this way that the change of the  $\text{Rh}^{4+}$  EPR mirrors the variation of the optical absorption along the vertical line in Fig. 1a at  $E_{\text{probe}} = 1.9$  eV. Therefore, an optical band with a maximum near 1.9 eV was ascribed to  $\text{Rh}^{4+}$ ; by consistency arguments those at 1.6 eV and 3.0 eV were shown to be due to the EPR-silent charge states  $\text{Rh}^{5+}$  and  $\text{Rh}^{3+}$ , respectively [10]. This assignment fulfills the features of the ‘three-valence model’ [14] (Fig. 2): the pump photon is absorbed in a primary step, in this way exciting a valence-band electron to the  $\text{Rh}^{3+/4+}$  level, creating  $\text{Rh}^{3+}$ , while the hole left in the valence band is captured by another  $\text{Rh}^{4+}$  ion, leading to  $\text{Rh}^{5+}$ . This sequence is summarized by  $2\text{Rh}^{4+} \rightarrow \text{Rh}^{3+} + \text{Rh}^{5+}$ . Such a scheme leads to photochromicity, as observed, since the metastable trapping of the transferred electrons means that the defect valencies have changed.

It is one of the advantages of the present method that in principle all relevant defects in a material can be taken into account in detail, i.e. here also those related to Fe. In previous studies this was not possible [12, 13], or such ions were considered only in a qualitative way [10]. In a way analogous to the Rh procedure a weak absorption structure near 2.3 eV is assigned to background  $\text{Fe}^{5+}$  [22], while the EPR-silent charge state  $\text{Fe}^{4+}$  is attributed to an absorption band near 2.8 eV. The absorption of  $\text{Fe}^{3+}$ , expected at 3.5 eV or higher [25], is covered by the fundamental absorption. All absorption features appearing in the landscape of Fig. 1a are assigned in this way to the indicated defect charge states. The pronounced changes occurring for  $E_{\text{pump}} > 2.5$  eV, not significant in the present context, are attributed to the light-induced creation of electrons and holes, captured at low temperatures at levels close to the conduction- and valence-band edges, respectively, leading to  $\text{Ti}^{3+}$ - and  $\text{O}^-$ -type EPR spectra [26]. At room temperature a part of these carriers recombines; another is trapped at deeper defects. For instance, holes are accommodated at  $\text{Rh}^{4+}$ , leading to the strong rise of  $\text{Rh}^{5+}$  under  $E_{\text{pump}} > 2.5$  eV, Fig. 1a.

### 2.3 Determination of the defect concentrations

The next aim is to determine the absorption cross sections of each of the indicated defect absorption bands quantitatively. This will allow us to infer the defect concentrations from the optical data. First, it is realized that optical

absorption bands, which are wide mainly because of strong carrier coupling to the lattice, are represented by functions of the type [27, 28]

$$\alpha(E) = CNEf(E). \quad (1)$$

Here  $C$  is a constant,  $N$  the defect concentration,  $E$  stands for  $E_{\text{probe}}$ , and  $f(E)$  is a Gaussian-type shape function [27]. In the previous work on BT:Rh [10] the proportionality of  $\alpha(E)$  to  $E$  was mistakenly not considered. The optical absorption features appearing in the entire plane of Fig. 1a can be analyzed with a maximal deviation  $\Delta\alpha < 10^{-3} \text{ cm}^{-1}$  into bands of the indicated type, their forms being shown in Fig. 4. An example is given in Fig. 3, where the absorption change  $\Delta\alpha$  reached after pumping with  $E_{\text{pump}} = 2.4$  eV is analyzed into five component bands:

$$\Delta\alpha(E) = C \sum_{i=1}^5 N_i E f_i(E). \quad (2)$$

Here  $i$  indicates the features attributed to  $\text{Rh}^{5+}$ ,  $\text{Rh}^{4+}$ ,  $\text{Rh}^{3+}$ ,  $\text{Fe}^{5+}$ , and  $\text{Fe}^{4+}$ , respectively. Since analogous decompositions can be made for any of the pump energies by using the same component bands, these are determined quite uniquely. In addition to treating these light-induced absorption changes  $\Delta\alpha$ , it is also possible to decompose the total absorptions  $\alpha$  into the same bands. It should be noted that the investigation of BT crystals containing only Fe leads to identical  $\text{Fe}^{4+}$  and  $\text{Fe}^{5+}$  band shapes, as expected.

The optical absorption function of defect  $i$ ,  $\alpha_i(E)$  or  $\Delta\alpha_i(E)$ , can be written alternatively as

$$\alpha_i(E) = S_i(E)N_i \quad \text{or} \quad \Delta\alpha_i(E) = S_i(E)\Delta N_i, \quad (3)$$

where  $S_i$  is the respective absorption cross section. Its shape is given, from comparison with (1), by

$$S_i(E) = CEf_i(E) \quad (4)$$

and has been obtained using the above fitting procedure. We start by determining the absolute values of the  $S_i(E)$  from the measured  $\Delta\alpha_i(E)$  by finding the defect concentrations  $\Delta N_i$ .

This task begins with the determination of the density of the EPR-active defects. By comparing the EPR signals (or their changes) of these defects with those of a  $\text{CuSO}_4 \cdot 5\text{H}_2\text{O}$  EPR standard, containing paramagnetic  $\text{Cu}^{2+}$  (spin  $S = 1/2$ ), of known mass and therefore of known number of spins, the concentrations of these defects (or their changes) are inferred according to an evaluation procedure given e.g. by Weil et al. [29]. In this way the concentration changes  $\Delta N_i$  of the EPR-active charge states  $\text{Rh}^{4+}$ ,  $\text{Fe}^{5+}$ , and  $\text{Fe}^{3+}$  are determined. Since the  $\Delta\alpha_i(E)$  functions of each of these centers have been identified before, the corresponding  $S_i(E)$  functions are now known.

The following strategy is used to determine the  $\Delta N_i(E)$  of the EPR-silent defects: since the total number of Rh and Fe impurities in a specific crystal is fixed (mass conservation) and assuming that 5+, 4+, and 3+ are the only valencies occurring for both elements, we have

$$\begin{aligned} \Delta\text{Rh}^{3+} + \underline{\Delta\text{Rh}^{4+}} + \Delta\text{Rh}^{5+} &= 0, \\ \underline{\Delta\text{Fe}^{3+}} + \Delta\text{Fe}^{4+} + \underline{\Delta\text{Fe}^{5+}} &= 0, \end{aligned} \quad (5)$$

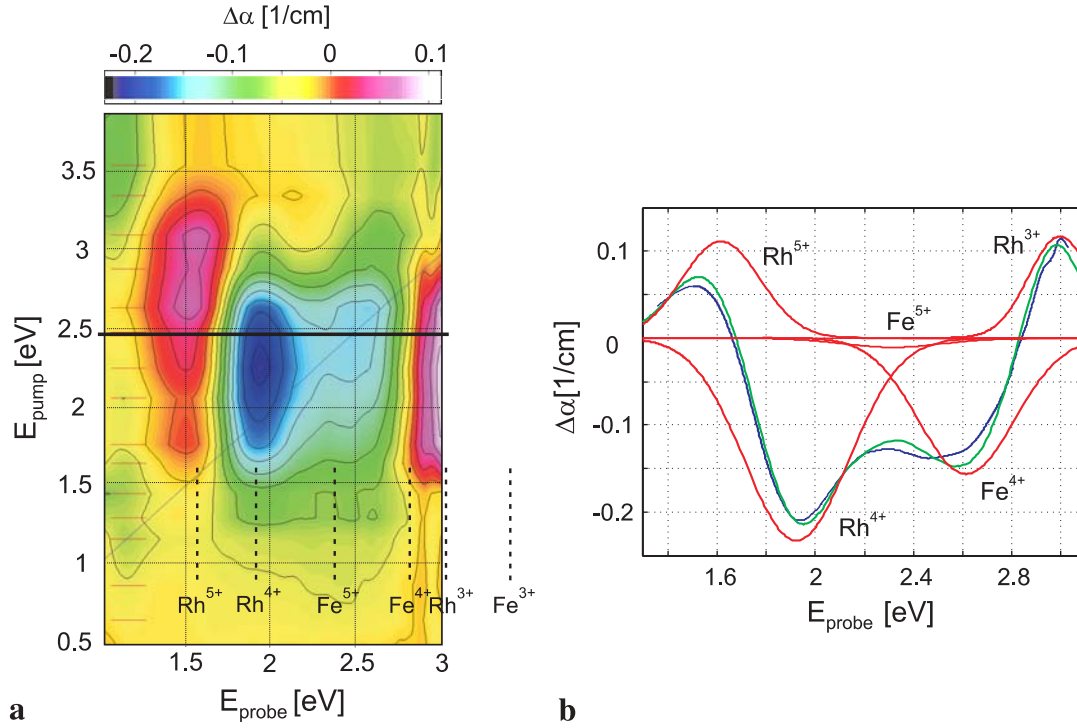


**FIGURE 3** Decomposition of the absorption changes induced by  $E_{\text{pump}} = 2.4 \text{ eV}$  (horizontal line in plot at left) into five functions of the type  $\alpha \sim E_{\text{probe}} f(E_{\text{probe}})$  (1), with a Gaussian shape function  $f(E)$ . The vertical dotted lines (at left) label the defects causing the features in the ‘landscape’, see text

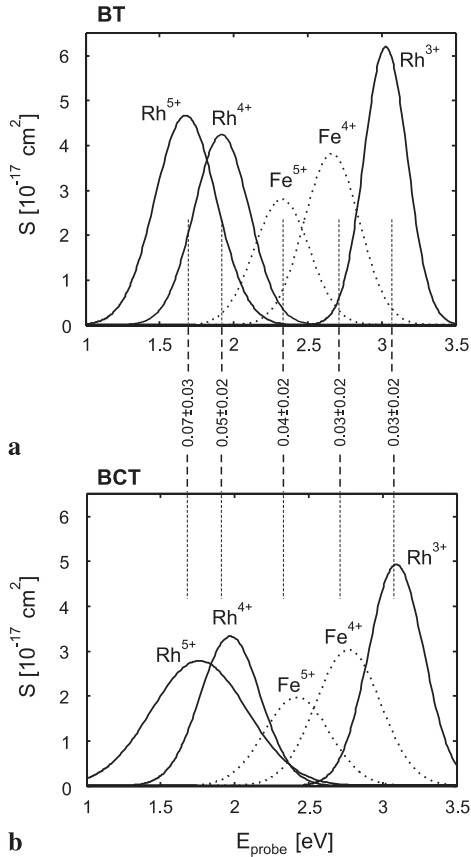


**FIGURE 4** Absorption cross sections of the indicated five defects for BT:Rh (a) and BCT:Rh (b). For BT:Rh the respective oscillator strengths, determined from EPR calibration, are indicated. They are transferred to the homologous defects in BCT

where the  $\Delta N_i$  are now replaced, in self-evident notation, by the corresponding chemical symbols. The concentrations of the EPR-active defects are underlined>. Another relation among concentration changes of the defects results from charge conservation; since only transfers via the valence band occur in the present case (Fig. 2), this is equivalent to hole conservation. This leads to

$$(\Delta \text{Rh}^{5+} - \Delta \text{Rh}^{3+}) + (\Delta \text{Fe}^{5+} - \Delta \text{Fe}^{3+}) = 0. \quad (6)$$

This equation is based on the following facts: (1)  $\text{Rh}^{4+}$  and  $\text{Fe}^{4+}$ , having charges equal to the replaced  $\text{Ti}^{4+}$ , are taken as reference states with no stored holes. (2) At each of the  $\text{Rh}^{5+}$  and  $\text{Fe}^{5+}$  sites one hole is stored, if compared to the 4+ reference states. A complementary reasoning holds for the 3+ valencies. (3) The light-induced transfer of the holes occurs only between the indicated Fe and Rh species. The donors and acceptors present in a crystal, serving to fix the initial equilibrium concentrations of the defects by compensating their charges, do not take part in the recharging process. This assumption is usually made [1].

From the above conservation equations, (5) and (6), the light-induced concentration changes  $\Delta N_i$  of the EPR-silent defects can be inferred, since those of the EPR-active ones had been determined directly, as explained before. Because all  $\Delta N_i$  are available now, the corresponding  $S_i(E)$  can be deduced from the measured  $\Delta \alpha_i$ . The resulting  $S_i(E)$  are plotted in Fig. 4 and the parameters defining their mathematical description in Table 5.

The integrated absorption cross sections are related to the oscillator strengths by Smakula’s equation (see e.g. [30]),

	BT	BCT
	Fe	Fe
$q_4^F$	$0.15 \pm 0.10$	$0.21 \pm 0.11$
$q_5^F$	1	1
$\gamma_3^F$	$(1.1 \pm 0.7) \times 10^{-13} \text{ cm}^3 \text{ s}^{-1}$	$(1.2 \pm 0.8) \times 10^{-13} \text{ cm}^3 \text{ s}^{-1}$
$\gamma_4^F$	$(3.3 \pm 2.5) \times 10^{-11} \text{ cm}^3 \text{ s}^{-1}$	$(2.6 \pm 1.7) \times 10^{-11} \text{ cm}^3 \text{ s}^{-1}$
$\beta_4^F$	$(2.8 \pm 2.1) \times 10^{-3} \text{ s}^{-1}$	$(2.4 \pm 1.7) \times 10^{-3} \text{ s}^{-1}$
$\beta_5^F$	$(1.2 \pm 0.9) \times 10^{-1} \text{ s}^{-1}$	$(1.0 \pm 0.7) \times 10^{-1} \text{ s}^{-1}$
	Rh	Rh
$q_4^R$	$0.02 \pm 0.01$	$0.009 \pm 0.006$
$q_5^R$	1	1
$\gamma_3^R$	$(1.7 \pm 0.8) \times 10^{-13} \text{ cm}^3 \text{ s}^{-1}$	$(2.8 \pm 2.1) \times 10^{-13} \text{ cm}^3 \text{ s}^{-1}$
$\gamma_4^R$	$(2.7 \pm 1.2) \times 10^{-11} \text{ cm}^3 \text{ s}^{-1}$	$(4.6 \pm 3.5) \times 10^{-11} \text{ cm}^3 \text{ s}^{-1}$
$\beta_4^R$	$(14.5 \pm 5.5) \times 10^{-3} \text{ s}^{-1}$	$(4.0 \pm 2.5) \times 10^{-3} \text{ s}^{-1}$
$\beta_5^R$	$(15.0 \pm 7.0) \times 10^{-1} \text{ s}^{-1}$	$(11.0 \pm 8.5) \times 10^{-1} \text{ s}^{-1}$
$p^{*,+}$	$(1.1 \pm 0.7) \times 10^{11} \text{ cm}^{-3}$	$(0.7 \pm 0.4) \times 10^{11} \text{ cm}^{-3}$
$p^{*,++}$	$(2.4 \pm 1.1) \times 10^{11} \text{ cm}^{-3}$	$(1.6 \pm 0.7) \times 10^{11} \text{ cm}^{-3}$

\* stationary hole density, calculated for a light energy of 1.96 eV and power densities of  $20^+$  and  $50^{++}$  mW/cm<sup>2</sup>

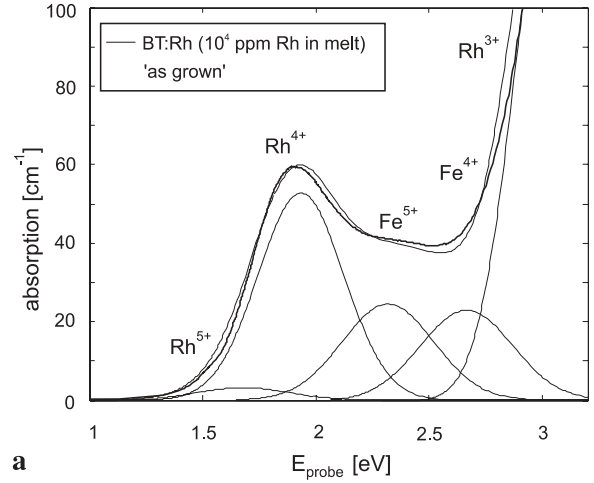
**TABLE 4** Parameters governing the light-induced charge transfers in BT:Rh, BT:Fe and BCT:Rh, BCT:Fe at room temperature

given here for the case of a Gaussian shape function:

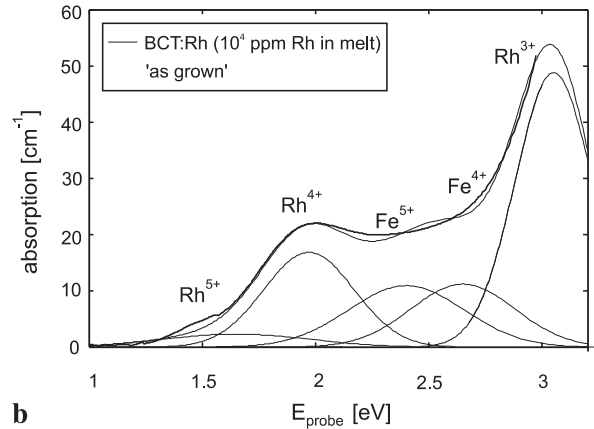
$$N_i f_i = 0.87 \times 10^{17} (n/(n^2 + 2)^2) \alpha_{\max,i} \Gamma_i \quad (7)$$

( $N_i$ : concentration of defect  $i$  in  $\text{cm}^{-3}$ ,  $f_i$ : the related oscillator strength,  $n$ : refractive index,  $\alpha_{\max,i}$ : maximal absorption coefficient of band  $i$  in  $\text{cm}^{-1}$ ,  $\Gamma_i$ : full width of band  $i$  at half maximum in eV). For the treated defects the derived oscillator strengths  $f_i$  are shown in Fig. 4 and in Table 5.

Using the absorption cross sections we determined the total concentrations of the defects  $\text{Rh}^{5+}$ ,  $\text{Rh}^{4+}$ ,  $\text{Rh}^{3+}$ ,  $\text{Fe}^{5+}$ , and  $\text{Fe}^{4+}$  by analyzing the total absorption spectra of BT:Rh (Fig. 5a). The results are listed in columns 4 to 6 and columns 8 to 10 of Table 3. These are based on the absorption spectra of the indicated BT:Rh crystals. It is seen that the values determined by the described optical procedure (see column 3 of Table 3) compare well, where possible, with those obtained directly by calibration of the EPR signals (see also column 3 of Table 3) of the EPR-active defect charge states. Furthermore, the total Fe and Rh concentrations, obtained by summing the  $\text{Fe}^{3+}$ ,  $\text{Fe}^{4+}$ , and  $\text{Fe}^{5+}$  and the  $\text{Rh}^{3+}$ ,  $\text{Rh}^{4+}$ , and  $\text{Rh}^{5+}$  densities, can be compared with the total Fe and Rh concentrations, known for crystals 'ob 1' and GR120 from quantitative chemical analyses; see columns 7 and 11 [31–33]. Both these



**a**



**b**

**FIGURE 5** Total absorptions at room temperature of BT:(10000 ppm Rh) (a) decomposed by the absorption cross sections indicated in Fig. 4. This leads to the defect concentrations listed in Table 3. **b** Same for BCT:(10000 ppm Rh)

cross-checks attest to the consistency and reliability of the method used. A general assessment of the errors involved in the procedure used will be given below. The results in Table 3 again [31] demonstrate the low distribution coefficient of Rh in BT; only between 1% and 3% of the Rh in the melt is found in the grown crystals, with a slight increase of incorporation with rising Rh in the melt. That of Fe, on the other hand, is high ( $\sim 50\%$ ), leading to considerable background concentrations even for low melt concentrations. Similar remarks will be seen to hold for BCT (Sect. 3).

	BaTiO <sub>3</sub>				Ba <sub>0.77</sub> Ca <sub>0.23</sub> TiO <sub>3</sub>		
	$S_{\max,i} [10^{-17} \text{ cm}^2]$	$E_{\max,i} [\text{eV}]$	$\Gamma_{\text{FWHM},i} [\text{eV}]$	oscillator strength	$S_{\max,i} [10^{-17} \text{ cm}^2]$	$E_{\max,i} [\text{eV}]$	$\Gamma_{\text{FWHM},i} [\text{eV}]$
$\text{Rh}^{5+}$	$4.6(\pm 2.2)$	$1.65(\pm 0.05)$	$0.45(\pm 0.10)$	$0.07(\pm 0.03)$	$2.7(\pm 1.3)$	$1.70(\pm 0.05)$	$0.75(\pm 0.20)$
$\text{Rh}^{4+}$	$4.1(\pm 2.0)$	$1.90(\pm 0.05)$	$0.35(\pm 0.10)$	$0.05(\pm 0.02)$	$3.2(\pm 1.6)$	$1.95(\pm 0.05)$	$0.45(\pm 0.10)$
$\text{Rh}^{3+}$	$6.0(\pm 2.4)$	$3.00(\pm 0.10)$	$0.30(\pm 0.10)$	$0.02(\pm 0.01)$	$4.9(\pm 2.2)$	$3.05(\pm 0.10)$	$0.40(\pm 0.10)$
$\text{Fe}^{5+}$	$2.7(\pm 1.3)$	$2.30(\pm 0.05)$	$0.40(\pm 0.10)$	$0.04(\pm 0.02)$	$2.0(\pm 1.0)$	$2.40(\pm 0.05)$	$0.60(\pm 0.10)$
$\text{Fe}^{4+}$	$3.9(\pm 1.9)$	$2.65(\pm 0.05)$	$0.40(\pm 0.10)$	$0.02(\pm 0.01)$	$3.0(\pm 1.5)$	$2.75(\pm 0.05)$	$0.60(\pm 0.10)$

$$S_i(E) = S_{0,i} \times E \times \exp\left(-\frac{4 \times \ln(2)}{\Gamma_{\text{FWHM},i}^2} \times (E - E_{\max,i})^2\right) \text{ with } S_{0,i} = S_{\max,i} / E_{\max,i}$$

**TABLE 5** Parameters of Gaussian bands describing the various absorption cross sections, as defined below the table (see also (4))

## 2.4 Quantitative determination of $N_{\text{eff}}$ and the charge-transfer parameters

Once the concentrations of the individual defects are known, further useful information can be deduced: at first we deal with the effective trap density  $N_{\text{eff}}$ , related to the space-charge fields  $E_{\text{sc}}$ . Then the parameters governing the charge-transfer processes will be determined. On this basis the photorefractive response times will be treated.

**2.4.1 Effective trap densities  $N_{\text{eff}}$ .** For a sinusoidal light pattern of wavevector  $k$ , impinging on a photorefractive material, in which the charge transport of the photoionized charge carriers is dominated by diffusion, the space-charge wave  $E_{\text{sc}}(k)$ , of course, is also characterized by the wavevector  $k$ , and its size is given by [34]:

$$E_{\text{sc}} = m \frac{k_{\text{B}}T}{e} \frac{k}{1 + \frac{k^2}{k_0^2}} \eta(I), \quad (8)$$

with  $m$ : degree of sinusoidal modulation of the light pattern;  $\eta(I) = (1 + I_{\text{sat}}/I)^{-1}$ : saturation factor;  $I_{\text{sat}} = \sigma_{\text{d}}/(\sigma_{\text{d}} + \sigma_{\text{ph}})$  ( $\sigma_{\text{d}}$  and  $\sigma_{\text{ph}}$ : dark conductivity and photoconductivity, respectively). Here

$$k_0^2 = e^2 N_{\text{eff}} / k_{\text{B}} T \epsilon_0 \epsilon_r = (2\pi / \Lambda_0)^2, \quad (9)$$

where  $\Lambda_0$  is the Debye screening length.  $N_{\text{eff}}$  is determined experimentally by finding the  $k$  value of the maximum of  $E_{\text{sc}}(k)$ . Equation (8) predicts that it occurs at  $k = k_0$  and thus allows us to infer  $N_{\text{eff}}$ . Theoretically,  $N_{\text{eff}}$  is given – for the superposition of two ‘three-valence’ systems symbolized in Fig. 2 – by

$$N_{\text{eff}} = N_{\text{eff}}^{\text{Rh}} + N_{\text{eff}}^{\text{Fe}}, \quad (10)$$

with

$$N_{\text{eff}}^{\text{Rh}} = \text{Rh}_{\text{tot}} - \text{Rh}^{4+}(I) - (1/\text{Rh}_{\text{tot}}) (\text{Rh}^{3+} - \text{Rh}^{5+})^2, \quad (11)$$

$$N_{\text{eff}}^{\text{Fe}} = \text{Fe}_{\text{tot}} - \text{Fe}^{4+}(I) - (1/\text{Fe}_{\text{tot}}) (\text{Fe}^{3+} - \text{Fe}^{5+})^2, \quad (12)$$

where the chemical symbols mean the concentrations of the respective defects. This is a generalization of a relation given

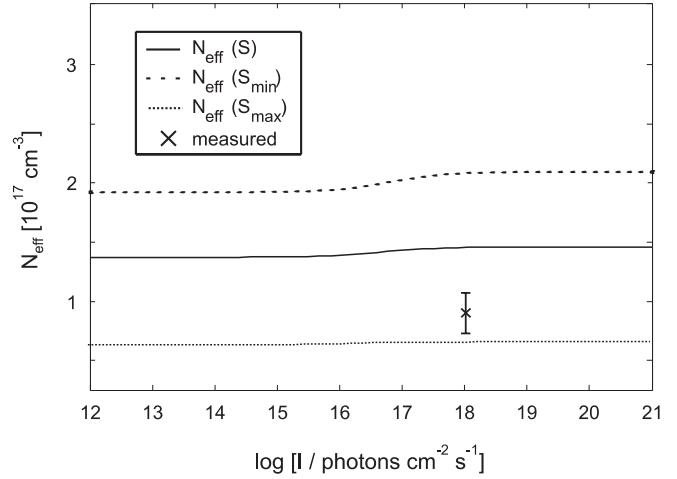


**FIGURE 6** Intensity dependence of the predicted  $N_{\text{eff}}$  for BT:Rh (crystal ‘ob1’) at a pump-light energy of 1.92 eV, as calculated by (10)–(12) based on data in Table 3 and Fig. 4a. The intensity  $I$  is given in (photons  $\text{cm}^{-2} \text{s}^{-1}$ ). The parameter uncertainties lead to the shown band of  $N_{\text{eff}}$ . The experimental  $N_{\text{eff}}$  [10] is marked as well; it is seen to lie within the error range. A corresponding plot has been shown in [10] on the basis of (1), where the factor  $E$  was not taken into account. The inclusion of this factor improves the coincidence between experiment and prediction

by Huot et al. [12] and was kindly communicated by Delaye [35]. It should be noted that here the homogeneous defect distribution, i.e. its zeroth-order Fourier component, enters, although  $E_{\text{sc}}$  in (1) is of first order [1]. All experimentally determined densities quoted in Table 3 are concerned with such homogeneous concentrations, and thus  $N_{\text{eff}}$  can now be calculated. The results are given in column 12 of this table. They are compared to the experimentally determined ones [10, 16]; see column 13. Where such data are available, a rather good coincidence is found. Apparently, the indicated EPR optical method is useful to predict the defect-related performance of the material.

The intensity dependence of  $N_{\text{eff}}$  ((10)–(12)), inferred below, is seen to be rather small (Fig. 6).

**2.4.2 Charge-transfer parameters.** Figure 7 shows how the concentrations of the Rh defects in a BT:Rh crystal (‘ob1’, see Table 2, column 1) adapt to changing illumination, when light is switched on (Fig. 7a) and off (Fig. 7b). Similar plots have

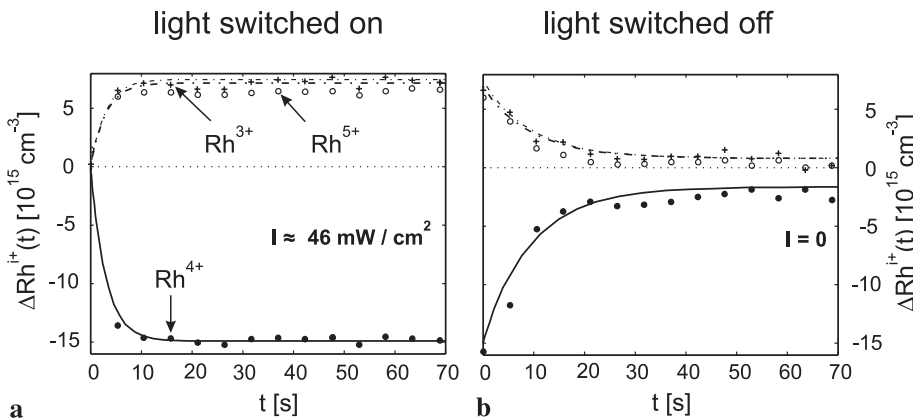


**FIGURE 7** Changes of the concentrations in ‘as-grown’ BT:Rh (crystal ‘ob1’, Table 2), after pump light ( $E_{\text{pump}} = 1.96$  eV) has been switched on (a) and switched off (b). The lines are optimally fitted solutions of the rate equations shown in Fig. 8b

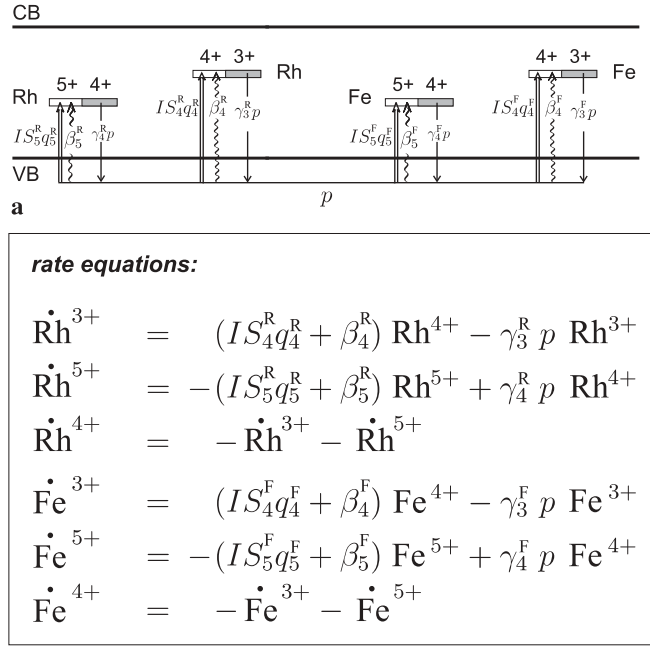


**FIGURE 8** **a** Hole-recharging processes among the indicated Rh and Fe defects. All defects are coupled by the reservoir of holes in the valence band. Wavy (straight double) arrows indicate thermally (optically) induced electronic excitations. Thermal and optical level positions are not distinguished. Wavy (straight double) arrows would end in thermal (optical) levels, if indicated. The energies of the thermal (optical) levels above the valence-band edge are:  $\sim 0.95$  eV (1.9 eV) for  $\text{Rh}^{3+/4+}$ ;  $\sim 0.7$  eV (1.6 eV) for  $\text{Rh}^{4+/5+}$ ;  $\sim 0.9$  eV (2.8 eV) for  $\text{Fe}^{3+/4+}$ ; and  $\sim 0.7$  eV (2.3 eV) for  $\text{Fe}^{4+/5+}$ . The energies of the thermal (optical) levels in BT are taken from [11] (this work).  $I$ : intensity;  $S$ : respective absorption cross section;  $q$ : quantum efficiency, i.e. probability that an absorbed quantum leads to ionization;  $\beta$ : thermal excitation rate;  $\gamma$ : recombination coefficient;  $p$ : hole density. **b** Rate equations corresponding to the scheme in the upper part

been obtained for the Fe changes. These concentration variations are based on the processes illustrated in Fig. 8a. They are cast into rate equations, which are a generalization of those given in [34], in Fig. 8b. Their numerical integrals can be fitted to the observed concentration changes by varying the parameters in the equations. In order to facilitate the fitting procedure it is subdivided into separate steps. First, the processes in crystals containing only Fe are analyzed. Since for  $I = 0$  only the parameters  $\gamma_3^F$ ,  $\gamma_4^F$ ,  $\beta_3^F$ , and  $\beta_4^F$  are relevant, these  $I = 0$  branches are fitted first. Then the values of  $q_4^F$  and  $q_5^F$  are taken from the Fe concentrations changing under  $I \neq 0$ . Using the parameters obtained in this way, crystals containing Rh – and background Fe – are studied. Again, first the parameters related to  $I = 0$  are identified and then the final ones determined by the situation  $I \neq 0$ . The parameters optimized in this way are presented in Table 4.

**2.4.3 Photorefractive response time.** For one of the investigated crystals, X17 in Table 2 and Table 3, the response time  $\tau_{sc}$  is known [16] to be 9 s, measured for long grating periods,  $k \sim 0$ , at an intensity of  $650 \text{ mW/cm}^2$  (at 850 nm). The response time is determined by the following relation [34, 36]:

$$\tau_{sc} = \tau_M \left( 1 + k^2/k_p^2 \right) / \left( 1 + k^2/k_0^2 \right), \quad (13)$$

with the Maxwell time  $\tau_M = \epsilon_0 \epsilon_r / \sigma$ .  $k_p$  is proportional to the inverse diffusion length of the holes, and all other parameters are as defined for (8) and (9). For the experimental situation,  $k \sim 0$ ,  $\tau_{sc} = \tau_M$ . The conductivity is given by  $\sigma = p e \mu$ , with  $p$  the hole density in the valence band and  $\mu$  the hole mobility. To obtain a representative value of  $p$ , it is estimated in the stationary state by setting all time derivatives in Fig. 8 equal to zero and employing the parameters from Table 3 in these equations. For an intensity  $20 \text{ mW/cm}^2$  at  $1.96 \text{ eV}$  (633 nm) a value  $p = 1.1 \times 10^{11} \text{ cm}^{-3}$  is found; for  $50 \text{ mW/cm}^2$ ,  $p = 2.4 \times 10^{11} \text{ cm}^{-3}$ . Both values are listed at the end of Table 4. (In the dark ( $I = 0$ ) the hole density is  $0.1 \times 10^{11} \text{ cm}^{-3}$ .) For the above intensity of  $650 \text{ mW/cm}^2$ , for which the quoted response time was measured at  $1.45 \text{ eV}$  (850 nm), a hole density  $p = 3.5 \times 10^{11} \text{ cm}^{-3}$  is calculated. On this basis the response time  $\tau_{sc} = 9 \text{ s}$  corresponds to a hole mobility  $\mu = 2 \times 10^{-4} \text{ cm}^2/\text{V s}$ . This lies in the range of values quoted previously [37].

### 3 Ba<sub>0.77</sub>Ca<sub>0.23</sub>TiO<sub>3</sub>:Rh

#### 3.1 Experimental details

BCT crystals grown from melts containing 1000, 2000, 4000, and 10 000 ppm Rh, respectively, were investigated; see column 1 of Tables 6 and 7. The method of crystal growth is outlined in [8]. Since it is possible [38] that Ca is not only incorporated on Ba but also on Ti sites, care was taken [8] to avoid this by preparing the melts with a Ti surplus,  $[\text{Ti}] > [\text{Ba} + \text{Ca}]$ . The conditions for oxidation and reduction were identical to those quoted for BT in Sect. 2.1. The photorefractive properties of crystals cut from the same boules have been investigated previously [7, 16].

Also, BCT:Rh crystals grown from melts containing up to 2000 ppm Na in addition were studied. No Na-specific features were identified. This is in accord with a neutron-activation analysis, indicating [39] that less Na is incorporated into the growing crystal in this way than the sensitivity limit of the method (15 ppm). So far the question is unanswered as to why BCT behaves so differently in comparison with BT, where Na is easily found in doped material by EPR [40] and where special purification techniques have to be applied to get rid of unintended Na in the material [41].

sample (crystal label)	doped with	doping (ppm in melt)	size [mm <sup>3</sup> ]	comment, treatment
BCT (B96)	Rh	1000	1.5 × 4.2 × 3.2	as grown <sup>+</sup>
(B97)	Rh	2000	1.4 × 5.3 × 3.0	as grown <sup>+</sup>
(B98)	Rh	4000	1.4 × 5.0 × 3.0	as grown <sup>+</sup>
(B99)	Rh	10 000	0.6 × 4.5 × 2.9	as grown <sup>+</sup>
(B99ox)	Rh	10 000	0.6 × 4.5 × 2.9	oxidized 2 h, 800 °C, 20 bar in O <sub>2</sub>
(B99red1)	Rh	10 000	0.6 × 3.5 × 3.4	reduced 2 h, 800 °C, 10 <sup>-3</sup> mbar
(B99red2)	Rh	10 000	0.6 × 3.5 × 3.4	reduced 2 h, 400 °C, 10 <sup>-4</sup> mbar
(B48)	Fe	77	1.6 × 4.4 × 4.3	as grown <sup>+</sup>

<sup>+</sup> chemical analysis available

**TABLE 6** List of BCT samples and their treatments



1 sample (lable)	2 doping (ppm)	3 Fe <sup>3+</sup> (ppm)	4 Fe <sup>4+</sup> (ppm)	5 Fe <sup>5+</sup> (ppm)	6 Fe <sup>tot</sup> (ppm)	7 Rh <sup>3+</sup> (ppm)	8 Rh <sup>4+</sup> (ppm)	9 Rh <sup>5+</sup> (ppm)	10 Fe <sup>tot</sup> (ppm)	11 $N_{\text{eff}}$ (pred.) $10^{17} \text{ cm}^{-3}$	12 $N_{\text{eff}}$ (meas.) $10^{17} \text{ cm}^{-3}$
BCT : Rh											
(B96)	1000	24.0	2.0	2.0	28 [32]	12.0	4.5	1.5	10 [33]	$1.8 \pm 1.2$	0.6 [16]
(B97)	2000	49.5	2.5	2.0	54 [33]	13.0	5.0	1.5		$1.9 \pm 1.3$	0.7 [16]
(B98)	4000	42.5	4.0	2.5	49 [33]	26.0	11.0	2.0	18 [33]	$2.8 \pm 1.7$	1.3 [16]
(B99)	10000	39.0	4.0	3.0	46 [32]	50.0	24.5	3.5	76 [33]	$5.4 \pm 3.4$	2.6 [16]
(B99ox)	10000	37.0	4.5	4.5	46 [33]	38.0	30.0	6.0	76 [33]	$6.0 \pm 4.0$	
(B99red1)	10000	> 44.5	1.0	< 1.0	46 [33]	~ 70.0	2.0	< 1.0	76 [33]	~ $1.0 \pm 0.6$	
BCT : Fe											
(B48)	77	65.0	2.0	1.0	68 [32]					$0.8 \pm 0.5$	

**TABLE 7** Concentrations of the Rh and Fe defects in BCT:Rh, doped with different amounts of Rh (in the melt), and the determined  $N_{\text{eff}}$ . The structure of the table is similar to that of Table 3. The defect concentrations could only be determined by optical means. Since Fe<sup>3+</sup> could not be monitored in this way, its concentration (column 3) is determined by deducing the measured Fe<sup>4+</sup> and Fe<sup>5+</sup> concentrations (columns 4 and 5) from the chemically determined Fe<sup>tot</sup> (column 6). All individual Rh densities can be determined optically and are compared to the total concentrations where available, determined chemically (column 10). The lowest two lines of the BCT:Rh section indicate the effect of oxidation and reduction on the concentrations

### 3.2 EPR of defects in BCT:Rh

While the results of EPR studies of defects in BT have been extensively documented [24, 42], less is known in this context about BCT. Special difficulties are encountered when defects in BCT are investigated by EPR. Here part of the Ba<sup>2+</sup> ions is replaced by the smaller Ca<sup>2+</sup> ions. At their twelfold-coordinated sites the respective ionic radii are 161 pm (Ba<sup>2+</sup>) and 134 pm (Ca<sup>2+</sup>) [43]. Ca is thus expected to go off-center, probably in uncorrelated directions. In this way possibly local dipoles are created with statistical orientations. Such dipoles and their relaxational behavior have been identified in the related compound Sr<sub>x</sub>Ca<sub>1-x</sub>TiO<sub>3</sub> [44], where the difference between the ionic radii is less extreme (Sr<sup>2+</sup>: 144 pm). In BCT the Ca disorder will have two types of effects on transition-metal ions, usually incorporated at Ti sites: off-center Ca ions next to such a transition-metal position tend to create low-symmetry crystal fields at such ions. Many such transition-metal–calcium configurations can be envisaged, each leading to a special type of low-symmetry EPR spectrum. Their superpositions cause complicated patterns, which are difficult to disentangle. If, on the other hand, the transition-metal ions happen to be surrounded in their first neighborhood by rather regular arrangements of Ba or Ca, the spatially fluctuating positions of the ions farther away will lead to inhomogeneous crystal fields, creating rather wide lines in optical and especially EPR spectroscopy. Furthermore, severe microwave damping is observed when studying BCT crystals in an EPR spectrometer; this is possibly caused by relaxation of the off-center dipoles.

In spite of these difficulties, several paramagnetic centers could be identified by EPR in the material [45]. The most pronounced ones result from the ubiquitous Fe background contamination. Four centers containing Fe<sup>3+</sup> were detected. Two of them have nearly cubic Fe<sup>3+</sup> surroundings. They can be ascribed to Fe<sup>3+</sup> replacing Ti<sup>4+</sup> at normal lattice sites, with two types of Ca associations. The third center is low-symmetry Fe<sup>3+</sup>, characterized by a moderately strong axial field directed along [100]-type directions approximately. The fourth center has a strong axial field, similar to that found previously [24] for Fe<sup>3+</sup> – V<sub>0</sub> pairs in BT. The center can thus tentatively be assigned to such a type of defect in BCT [45].

High-intensity illumination at low temperatures creates additional paramagnetic defects. For  $E_{\text{pump}} > 2.3$  eV these fall into mainly two classes, those of Ti<sup>3+</sup> type, i.e. electrons captured at levels close to the conduction band, and those typical for captured valence-band holes, leading to O<sup>-</sup> defects close to trapping defects. The essential threshold energy for this process is about 2.3 eV, similar to what has been found in BT [26].

Because of their strong sensitivity to strains, unfortunately neither of the EPR-active charge states Rh<sup>4+</sup> or Fe<sup>5+</sup> could be detected by EPR in BCT. The gross features of the EPR results found with BCT are consistent with those previously identified for BT. They show mainly that even in nominally undoped or Rh-doped crystals there is a strong background contamination by iron. Because paramagnetic centers in the well-ordered BT:Rh could be studied in more detail and because the relation to the relevant Rh and Fe optical spectra of these defects has been established previously, we thus transfer these optical results from BT:Rh to BCT:Rh and use them as the optical fingerprints of the defects occurring in the material. On this basis the light-induced defect-recharging processes in BCT will be elucidated.

### 3.3 Optical absorption bands of Rh and Fe in BCT:Rh

Figure 5b shows the room-temperature optical absorption of a BCT crystal, doped with 10 000 ppm Rh in the melt in its ‘as-grown’ state. Using an optimized decomposition into bands of the type defined in (1), five peaks are seen to contribute to the total absorption, which are assigned to three charge states of Rh and two of Fe, as shown. These same bands also lead to the best decomposition of the light-induced absorption changes of BCT, shown in Fig. 1c. The optimally fitting component bands, Fig. 4b, turn out to be quite similar to those obtained for BT:Rh, Fig. 4a. However slight shifts of the band maxima in BCT to higher energies are clearly seen. Also, the band widths are larger in BCT. The first feature might be caused by the somewhat lower lattice constants of BCT (Table 1), while the increased band widths can be attributed to the influence of disorder of the material.

BCT crystals containing only Fe, in which the optical bands of Fe<sup>5+</sup> and Fe<sup>4+</sup> could be monitored without interference with Rh absorptions, were studied separately. This leads

to an independent determination of the relevant iron bands, identical to those given in Fig. 4b. For an overview of the features introduced into BCT by Fe doping see [46].

In spite of the different Fe sites identified by the EPR studies of  $\text{Fe}^{3+}$  in the material, only one band has been assigned to each of the Fe charges appearing in the optical absorption spectra (Figs. 4b and 5b). Previous experience with absorption spectra of Fe in different surroundings indicates that this is not a contradiction. In studies of  $\text{Fe}^{4+}$  and  $\text{Fe}^{4+} - V_0$  in  $\text{SrTiO}_3$  [47], identified by EPR, it was noticed that rather similar absorption bands were observed in both cases. Analogous observations were made recently for  $\text{Fe}^{2+}$  and  $\text{Fe}^{3+}$  and its various associations in  $\text{KTaO}_3$  [25], where the absorption bands varied only a little depending on the different surroundings. While low-symmetry influences on a paramagnetic ion lead to profound variations of its EPR features, being sensitive to rather small ground-state splittings, the optical excitations are less affected by associations. Here the changes of the electronic levels, caused by low-symmetry influences, are comparatively small relative to the larger mean transition energies. These changes, however, tend to increase the line widths. As mentioned, this might explain why the optical line widths in BCT (Fig. 4b) are larger than those in the well-ordered BT (Fig. 4a).

### 3.4 Determination of the defect concentrations

Because EPR signals of  $\text{Rh}^{4+}$  and  $\text{Fe}^{5+}$ , observable in BT, cannot be detected in BCT and since the  $\text{Fe}^{3+}$ -related defects have rather wide and odd-shaped EPR spectra – their integration leading to large errors – quantitative information on defect concentrations cannot be derived from the EPR spectra for BCT. Since, however, the optical bands of BCT:Rh are quite similar to those of BT:Rh, we assume that the oscillator strengths, determined for each of the defects in BT:Rh (Fig. 4a), are equal to those in BCT:Rh. On the basis of Smakula's formula, (7), which connects the concentration of a defect with its oscillator strength, the defect densities can then be inferred. From these values the absorption cross sections, Fig. 4b, are deduced. Although the knowledge of the oscillator strengths, together with those of the band parameters  $\alpha_{\text{max}}$  and  $\Gamma$ , is sufficient to obtain the defect densities directly, we prefer to use the indirect method employing the derived absorption cross sections in the following, in order to keep the evaluation process in parallel to that used for BT:Rh.

Table 7 lists the concentrations determined in this way of the various Fe valencies (columns 3 to 5) and Rh defects (columns 7 to 9) in the investigated BCT samples. Also, the data pertaining to a crystal doped only with Fe are shown. Since, in contrast to BT, the concentrations of the  $\text{Fe}^{3+}$ -related defects cannot be taken from EPR (nor from optical studies) in BCT, here the determination of the total Fe defect densities, column 6, obtained from chemical analysis, has been used to infer the  $\text{Fe}^{3+}$  concentration (column 3) by subtracting the  $\text{Fe}^{4+}$  (column 4) and  $\text{Fe}^{5+}$  (column 5) densities from the  $\text{Fe}^{\text{tot}}$  values in column 6. The densities of  $\text{Rh}^{3+}$ ,  $\text{Rh}^{4+}$ , and  $\text{Rh}^{5+}$ , on the other hand, are all available from the described optical studies. Their sums compare rather favorably with the chemically determined total concentrations (column 10), where available.

Knowing the defect densities, the component bands were translated into the absorption cross sections, Fig. 4b. This offers the opportunity to analyze further optical absorption data also, such as the light-induced absorption changes, with respect to the defect concentrations involved in the specific studied cases.

### 3.5 Determination of $N_{\text{eff}}$ , the charge-transfer parameters, and the response times

From the data in Table 7 (columns 3 to 5 and columns 7 to 9) the values of  $N_{\text{eff}}$  are calculated (Table 7, column 11), using (10)–(12). Considering the indirect way in which the BCT defect concentrations are evaluated, the comparison with the experimental values of  $N_{\text{eff}}$  (column 12) still shows a remarkable coincidence, much better than an order of magnitude.

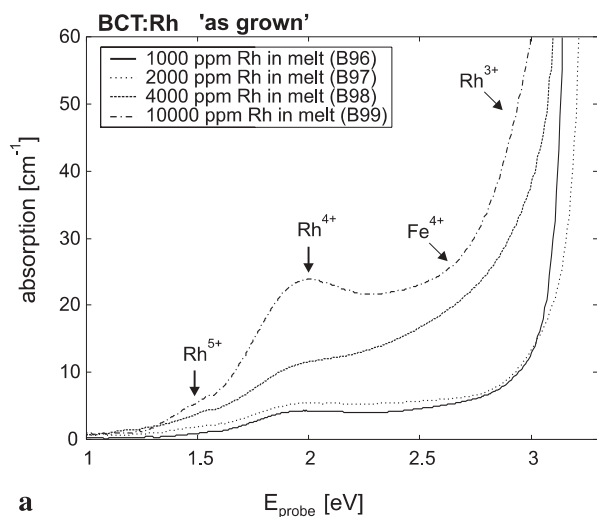
The time-dependent light-induced absorption changes in BCT, translated into the related concentration variations, are studied in a way analogous to that used for BT (Sect. 2.4.2). The obtained charge-transfer parameters are listed in Table 4, right-hand side. These values are comparable to those determined for BT:Rh. They thus appear to be plausible, supporting the method by which they are derived.

For the BCT crystals B96 and B97, values of the response times  $\tau_{\text{sc}}$  are available [16], measured with 850-nm light, an intensity of  $1 \text{ W/cm}^2$ , and long grating periods: they are 9 s for B96 and 8 s for B97. A rough estimate of the hole densities, calculated with the mean values of the parameters in Table 4 and the absorption cross sections in Fig. 4b, leads to  $1.6 \times 10^{11} / \text{cm}^3$  and  $1.7 \times 10^{11} / \text{cm}^3$  for both crystals under the indicated illumination. This is accord (see Sect. 2.4.3) with the measured Maxwell times  $\tau_{\text{M}}$  for a mobility in the range of  $10^{-4} \text{ cm}^2/\text{V s}$ . Within the estimate, the mobility is the same as that found for BT:Rh.

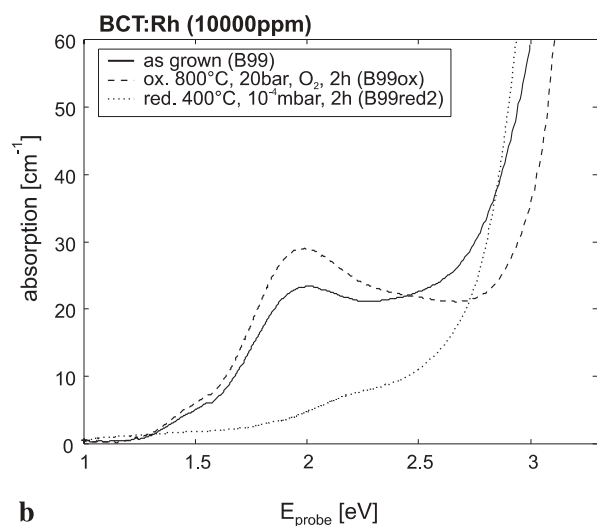
### 3.6 Further analysis of the absorption spectra of BCT:Rh and BT:Rh

In Fig. 9a the sequence of spectra of the total absorptions of all investigated BCT:Rh crystals in their 'as-grown' state is shown. From these spectra and also from Tables 3 and 7 it can be seen that the  $\text{Rh}^{4+}$  absorptions do not increase proportionally to the Rh content in the melts; see also [7]. Only starting at 4000 ppm can a clear increase of the  $\text{Rh}^{4+}$  absorption near 1.9 eV and that of  $\text{Rh}^{3+}$  close to the fundamental absorption edge be discerned. These bands, however, are not separated distinctly from each other, but are connected by a wide 'bridge' between 2.0 and 2.8 eV. As suggested by Fig. 5, this 'bridge' is decomposed into absorption bands attributed to  $\text{Fe}^{4+}$  and  $\text{Fe}^{5+}$ . Similar features are observed with the investigated BT:Rh crystals, Fig. 10a.

In Fig. 9b and Table 6 the reduction/oxidation behaviors of BCT crystals, grown from melts with 10 000 ppm Rh, are compared. It is seen that oxidation shifts the absorption edge to higher energies. Quite similar changes are observed for BT:Rh, Fig. 10b. This must certainly be attributed to a decrease of the  $\text{Rh}^{3+}$  concentration, since simultaneously the  $\text{Rh}^{4+}$  content rises. Also, a small increase of  $\text{Rh}^{5+}$  is seen. The opposite behavior is observed under weak reduction at  $400^\circ\text{C}$ : the energy of the absorption edge is lowered, caused



a



b

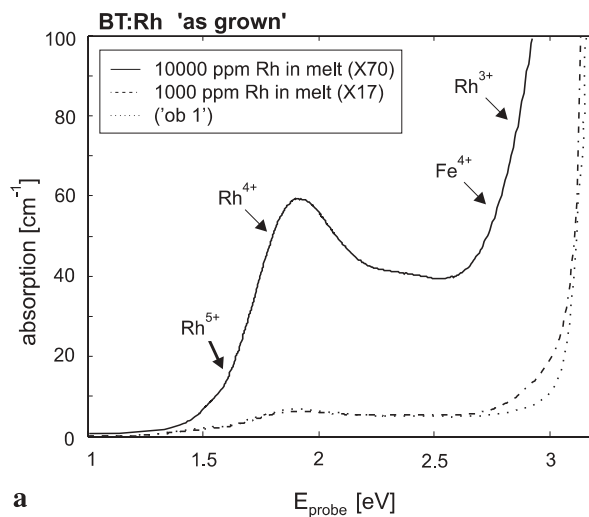
**FIGURE 9** **a** Room-temperature optical absorptions of (multidomain) BCT crystals with the indicated Rh contents in the melts. Only Rh contents larger than 2000 ppm lead to pronounced Rh-related bands. **b** Dependence of the optical absorption of BCT:(10000 ppm Rh) on oxidation and reduction

by a rising  $\text{Rh}^{3+}$  content, and the  $\text{Rh}^{4+}$  and  $\text{Rh}^{5+}$  concentrations decrease. These qualitative arguments are supported quantitatively in Table 7. It should be added that reduction at a higher temperature, 800 °C, leads to an optical band, not shown, with a maximum at 2.7 eV, which can possibly be attributed to the association of a so far unknown Rh charge state with an oxygen vacancy.

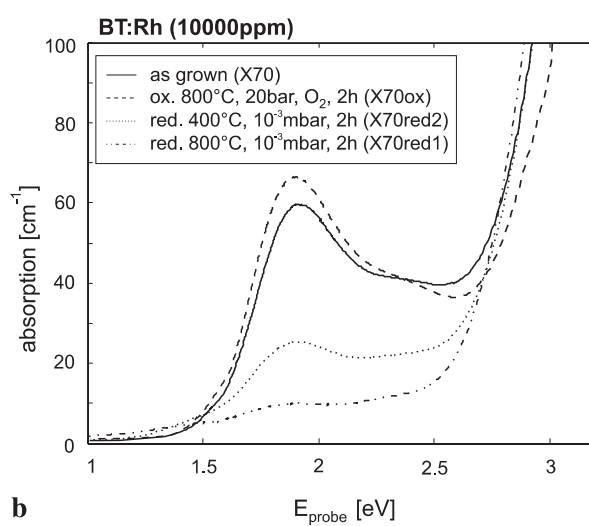
#### 4 Further observations

##### 4.1 On the decay of the light-induced-absorption changes

In Fig. 7b it is seen that the light-induced concentration changes of BT:Rh do not decay completely to the initial state,  $\Delta N_i = 0$ , if the illumination is stopped, but remain at about 8%. In BCT the corresponding long-time level is about 30%. The final decay relaxation takes days at room temperature and has not been analyzed in detail. The phenomenon is certainly to be attributed to disorder in the crystals, larger in BCT than in BT. For an explanation it must be considered that it is mainly the thermal ionization of  $\text{Rh}^{5+}$  under



a



b

**FIGURE 10** **a** Total absorptions at room temperature of the indicated (multidomain) BT crystals (Table 2, column 1). **b** Total absorptions of BT:(10000 ppm Rh) under the indicated reduction and oxidation treatments

$I = 0$  which furnishes the holes which eventually recombine with  $\text{Rh}^{3+}$ , leading to the equilibrium concentrations  $\Delta N_i = 0$  (see Fig. 7). A spatial variation of the depth of the  $\text{Rh}^{4+/5+}$  levels might be one cause for the observed behavior. A corresponding argument holds for the Fe charge states. However, the influence of disorder on the hole mobility is expected to be more decisive. Because short-time and long-time equilibrations must be distinguished, it appears that the mobility is determined by two types of influences. As a model it can be assumed that recombination in less disordered regions must be separated from that in more disordered ones. Only in the less disordered regions will the holes reach the  $\text{Rh}^{3+}$  and  $\text{Fe}^{3+}$  recombination centers quickly, causing the fast initial decay. High disorder tends to localize the holes, possibly leading to shallow traps. Only the initial decay is the basis for the recombination parameters in Table 4; it could be shown that assumed variations of the slow behavior influence the parameters listed in Table 4 only within the given limits of error.

Corner et al. [13], likewise investigating the decay of light-induced-absorption changes in BT:Rh, have also observed

that a short decay is accompanied by a rather long one. In evaluating the decay behavior with equations analogous to those in Fig. 8, they also took into account only the initial fast branch.

#### 4.2 On the reliability of the obtained results

At various points it has been demonstrated that the obtained results are internally consistent, e.g. with respect to the congruence of defect-density data obtained with optical and EPR methods and their agreement with chemical analysis results for BT:Rh mentioned at the end of Sect. 2.3. For BCT similar observations have been listed near the end of Sects. 3.4 and 3.5. Thus the method appears to furnish reliable results, in spite of the somewhat indirect evaluation paths involved.

In the following we comment on the possible sources of errors. For BT:Rh these are mainly: (1) the determination of the  $\text{Rh}^{4+}$ ,  $\text{Fe}^{3+}$ , and  $\text{Fe}^{5+}$  EPR intensities and their calibration in absolute concentrations by comparison with the EPR standard; (2) the comparison of the changes of the EPR intensities with those of the light-induced absorptions; (3) the decomposition of the absorption features into bands of the type given by (1); (4) the fitting of the rate-equation parameters (Fig. 8) to the measured time dependences of the light-induced-absorption changes (Fig. 7). Errors of about 50% included in Table 3 are assumed to take account of these items. Since the evaluation of the BCT data depends on the transfer of the BT oscillator strengths, a further source of error is present. Therefore, the BCT values tend to have larger error ranges.

## 5 Discussion

The new experimental method, on which the paper is based, has been developed here to its most general scope. In its basic stage it allows the qualitative elucidation of the light-induced charge transfers between defects in a photorefractive or, rather, photochromic, material. Its second stage, realized here, permits the quantitative determination of the various defect concentrations in the individual crystals as well as the complete set of charge-transfer parameters, globally valid for a certain photorefractive material with a definite doping. The method is applied here to BT:Rh and to BCT:Rh crystals. All data are based on EPR studies, mediated if necessary by accompanying optical absorption studies. At present, we do not see any other procedure to arrive at such results. Previously, charge-transfer parameters have been inferred from measured values of  $N_{\text{eff}}$ , supported by investigations of light-induced absorptions [12, 13]. Since this represents a rather limited information, more simple expressions than the general ones in Fig. 8 had to be used for the evaluation of the data. Especially, the quantum efficiencies  $q_i$  were assumed to have the values 1 throughout, and not all defect charge states, such as  $\text{Fe}^{5+}$ , were taken into account. Furthermore, in these studies the values of  $N_{\text{eff}}$  could not be predicted. The experimental  $N_{\text{eff}}$  were rather used as an input for the evaluation. Here we have a series of independent information on the defect densities and are thus able to predict  $N_{\text{eff}}$  and the related aspects of the photorefractive performance of the materials.

It has to be stressed that the method in no way is restricted to the studied sample cases, BT:Rh and BCT:Rh. These serve

here as examples for the scope of the method, which can be applied to all photochromic materials, not only photorefractive ones, where information on light-induced EPR changes is available simultaneously with that on the optical absorption changes.

In the following we list further advantages of the method. (1) After determination of the absorption cross sections at low temperatures, where the density-calibrating EPR investigations have to be performed generally, these absorption data can be transferred with little error to room temperature. The resulting uncertainties are small since the optical bands are intrinsically wide because of carrier-phonon coupling. Compared to that the increase of the bandwidths with rising temperature is negligible. Thus the method allows us to characterize photorefractive materials at room temperature, where such devices are expected to operate and where, however, direct EPR investigations in contrast to optical ones usually are impossible. (2) The investigations can be performed with multidomain crystals; poling of the specimens, needed for photorefractive studies, is thus not required. (3) The plots representing the photochromic behavior of the materials, Fig. 1, can be used for a fast room-temperature assessment of the defect content of a specific material, of the optical response of their changes, and the responsible charge-transfer processes. Since, as inferred from experience, such ‘landscapes’ (see e.g. Fig. 1) vary slightly from crystal to crystal, even if these are cut from the same boule, they can be used for a quality check of the crystals, giving hints to their improvement. This offers a basis on which a systematic investigation concerning the interrelation between crystal quality, depending on the mode of preparation, and the photorefractive performance of e.g. BT:Rh could be started. Such studies would have extended beyond the scope of the present work and have thus not yet been attempted.

It has to be pointed out that the oscillator strengths of the bands are rather high (Fig. 4), as compared with the physically highest possible value 1; this is expected for charge-transfer excitations. Internal transitions between defect levels, such as crystal field excitations, essentially of  $d-d$  type, are largely parity forbidden and should be much weaker. Therefore, they were not considered in the analysis of the optical absorption spectra.

A few remarks concerning the transfer parameters in Table 4 are appropriate. For the thermal ionization parameters the relation  $\beta_4 \ll \beta_5$  holds, since the corresponding charge states belong to the deeper and more shallow thermal levels, respectively; see Fig. 8a. The recombination coefficients  $\gamma$  for both Rh and Fe are related to those of the corresponding  $\beta$  values by the mass-action relations derived from Fig. 8b for  $I = 0$ . For thermal equilibrium all time derivatives are zero and therefore  $(\beta_5^R \gamma_3^R) / (\beta_4^R \gamma_4^R) = (\text{Rh}^{4+})^2 / (\text{Rh}^{5+})(\text{Rh}^{3+})$  and for the Fe defects correspondingly. This relation should be globally valid, i.e. independent of the existing defect concentrations in all crystals. Indeed the mass-action constant is found to be roughly 1 for the Rh concentrations for all Rh entries of Tables 3 and 7, and about 0.1 for the Fe entries. The ionization probabilities  $q_i$  are mainly determined by the overlap of the optically excited defect states with the valence-band Bloch waves; the larger the overlap, the higher the probability for an excited hole to diffuse away. Because of the lower en-

ergy distance of the  $\text{Rh}^{5+}$  and  $\text{Fe}^{5+}$  levels to the valence band, the corresponding wavefunctions are expected to be farther extended than those of  $\text{Rh}^{4+}$  and  $\text{Fe}^{4+}$ . This may explain why the  $q_5$  parameters are so much larger than the  $q_4$ . It should be noted that the  $q_4$ , even if small, must not be taken to be zero in order to obtain a fit to the time dependences in Fig. 7.

As stated above, previous investigations [12, 13, 48] of the transfer parameters in BT:Rh employed experimental methods providing much less information than the procedure which we use here. All the information on the defect densities had to be taken from photorefractive measurements yielding the single quantity  $N_{\text{eff}}$ , which comprises all charge states of Rh; see (11). The presence of Fe as background impurities was not considered in these investigations. From the present EPR-based studies, on the other hand, we could obtain the individual Rh defect concentrations separately. It is thus not surprising that the previous limited knowledge about the system tended to lead to different values of the Rh-related parameters than those listed in Table 5. The most important difference to the present results is the relation  $\gamma_3/\gamma_4 > 1$ , quoted in all these studies [12, 13, 48]. According to the arguments given in the previous paragraph, this is not consistent with the validity of the mass-action relation and the fact that  $\beta_5 \gg \beta_4$ , for Rh as well as for Fe. Since the mass-action constant is about 1 for all Rh crystals, this requires  $\gamma_3^R/\gamma_4^R < 1$  for BT:Rh. The recombination parameters  $\gamma_i$  obtained by us (Table 4) fulfill this required sequence. Since the  $\beta_i^R$  values are rather directly accessible in the earlier experiments also, such values reported previously are roughly comparable with ours; the discrepancies thus result from the  $\gamma_i^R$ .

Further differences are found for the absorption cross sections  $S$  (Fig. 4 and Table 5). Huot et al., for example, reported  $1.2 \times 10^{-5} \text{ m}^2/\text{J}$  (at  $1.06 \mu\text{m}$ ) for  $S(\text{Rh}^{4+})$  [12], corresponding to  $3 \times 10^{-20} \text{ cm}^2$  (per photon), whereas our analysis yields  $2 \times 10^{-18} \text{ cm}^2$ , about two orders of magnitude larger. This difference is mainly caused by the fact that we could determine the quantum efficiencies  $q_i$  separately from the products  $q_i S_i$ . Because of limited information in the previous studies [13, 48],  $q_i = 1$  was assumed for all  $q_i$ . Since absorption is not necessarily connected with ionization, this is not justified a priori. Since the  $q_i$  are always appearing (Fig. 8) in the products  $q_i S_i$ , the derived absorption cross sections were affected by the initial choice of the  $q_i$ . By our method we have enough information to determine the  $q_i$  individually. It can be seen as a further advantage of our evaluations that they lead to the total energy dependence of the  $S_i$  (Fig. 4). In the previous investigations only  $S_i$  values for selected energies were given.

Bernhardt et al. [7] discovered that rather high intensities  $I$  have to be applied to BCT:Rh in order that the factor  $\eta(I)$  in (8) approaches its saturation value 1. For BCT:(1000 ppm Rh) (B96), as an example, the saturation intensity  $I_{\text{sat}}$  was found to be about 100 times higher than for BT:(1000 ppm Rh) (X17). The authors attributed this to the higher Fe background contamination, increasing the dark conductivity, presumed to be present in BCT:Rh. Indeed, we identify somewhat larger Fe concentrations in BCT:Rh than in BT:Rh (compare Tables 3 and 7). The difference, however, is not sufficient to explain the higher saturation intensity. Bernhardt et al. had to postulate a Fe density of  $64 \times 10^{17} \text{ cm}^{-3}$  [7] ( $\sim 400$  ppm) for specimen B96 (1000 ppm Rh) in Table 4, in order to ex-

plain the high value of  $I_{\text{sat}}$ , whereas the chemical analysis finds only 28 ppm total Fe in crystals grown from the same boule. The argument of Bernhardt et al. [7], however, takes only one Fe level into account, defined by  $\text{Fe}^{3+/4+}$ . Considering in addition the shallow  $\text{Fe}^{4+/5+}$  level can predict higher values of  $I_{\text{sat}}$  for the same total Fe concentrations. Even under this consistent treatment, however, the available crystal data do not reproduce the measured high saturation intensities for BCT. Therefore, another reason must be found to explain this phenomenon. The presence of shallow, disorder-induced hole traps, not considered so far in detail, could possibly account for the discrepancy. A definite proof for this model, however, still is lacking. Optical absorption signals peaked at energies below the  $\text{Rh}^{5+}$  band have sometimes been observed in BCT:Rh – and not in BT:Rh – after illumination, but a consistent, reproducible behavior could not be distilled so far from the observed phenomena. The observed low absorption energies are expected for shallow hole traps, as investigated for instance in BT:Na [40]. Corresponding EPR signals could not be identified in BCT:Rh.

It has been pointed out by Roosen et al. [49] that the general properties of BCT:Rh, in spite of its high saturation intensity, still recommend the material as a favorable replacement of BT:Rh in those cases where the detrimental influence of the tetragonal–orthorhombic phase transition of the latter poses a problem for applications.

## 6 Conclusion

An experimental route has been drawn from the defects in a photorefractive material to its performance. It is based on a combination of EPR and optical absorption studies and leads to the most detailed conceivable quantitative information involved in the processes determining the space-charge fields. The method has a more general scope than the application to the special cases BT:Rh and BCT:Rh presented here. It is expected that the improvement of these and also further photorefractive materials will be supported by the use of the procedures outlined here.

**ACKNOWLEDGEMENTS** We thank M. Kaczmarek for lending some BT crystals and communicating photorefractive data measured with them. P. Delaye kindly made available a theoretical derivation of the effective trap densities expected for two combined ‘three-valence’ systems. We further are grateful to him and S. Bernhardt for numerous exchanges of ideas concerning the photorefractive behavior of BCT. In addition, we wish to thank H. Hesse and D. Rytz for supplying the other BT:Rh crystals studied and for many clarifying discussions. We remember with pleasure cooperation with V. Grachev and G. Malovichko. The permanent help and support by W. Koslowski is gratefully acknowledged. Part of this work has been supported by SFB 225 and TFB 13, both funded by DFG.

## REFERENCES

- 1 See e.g. K. Buse: Appl. Phys. B **64**, 391 (1997)
- 2 H. Veenhuis, T. Börger, K. Peithmann, M. Flaspöhler, K. Buse, R. Pankrath, H. Hesse, E. Krätzig: Appl. Phys. B **70**, 797 (2000)
- 3 G.W. Ross, P. Hribek, R.W. Eason, M.H. Garrett, D. Rytz: Opt. Commun. **101**, 60 (1993)
- 4 B.A. Wechsler, M.B. Klein, C.C. Nelson, R.N. Schwartz: Opt. Lett. **20**, 1850 (1994)
- 5 M. Kaczmarek, R.W. Eason: Opt. Lett. **20**, 1850 (1995)
- 6 S. Bernhardt, H. Veenhuis, P. Delaye, G. Roosen: Opt. Mater. **18**, 13 (2001)

- 7 S. Bernhardt, H. Veenhuis, P. Delaye, R. Pankrath, G. Roosen: Appl. Phys. B **74**, 287 (2002)
- 8 C. Kuper, R. Pankrath, H. Hesse: Appl. Phys. A **65**, 301 (1997)
- 9 C. Kuper, K. Buse, U. van Stevendaal, M. Weber, T. Leidlo, H. Hesse, E. Krätzig: Ferroelectrics **208**, 213 (1998)
- 10 C. Veber, M. Meyer, O.F. Schirmer, M. Kaczmarek: J. Phys.: Condens. Matter **15**, 415 (2003)
- 11 U. van Stevendaal, K. Buse, S. Kämper, H. Hesse, E. Krätzig: Appl. Phys. B **63**, 315 (1996)
- 12 N. Huot, J.M.C. Jonathan, G. Roosen: Appl. Phys. B **65**, 489 (1997)
- 13 L. Corner, R. Ramos-Garcia, A. Petris, M.J. Damzen: Opt. Commun. **143**, 165 (1997)
- 14 K. Buse, E. Krätzig: Appl. Phys. B **61**, 27 (1995)
- 15 H. Kröse, R. Scharfschwerdt, O.F. Schirmer, H. Hesse: Appl. Phys. B **61**, 1 (1995)
- 16 S. Bernhardt: PhD thesis, Université de Paris XI (2001); private communication (2003)
- 17 A. Radoua, P. Delaye, R. Pankrath, G. Roosen: J. Opt. A: Pure Appl. Opt. **5**, S477 (2003)
- 18 A. Mazur, O.F. Schirmer, S. Mendricks: Appl. Phys. Lett. **70**, 2395 (1997)
- 19 A. Mazur, C. Veber, O.F. Schirmer, C. Kuper, H. Hesse: Radiat. Eff. Defects Solids **150**, 281 (1999)
- 20 O.F. Schirmer: Radiat. Eff. Defects Solids **149**, 1 (1999)
- 21 A. Rüdiger, O. Schirmer, S. Odoulov, A. Shumelyuk, A. Grabar: Opt. Mater. **18**, 123 (2001)
- 22 O.F. Schirmer, M. Meyer, A. Rüdiger, C. Veber: Opt. Mater. **18**, 1 (2001)
- 23 H. Kröse, R. Scharfschwerdt, A. Mazur, O.F. Schirmer: Appl. Phys. B **67**, 79 (1998)
- 24 E. Possenriede, J. Jacobs, O.F. Schirmer: J. Phys.: Condens. Matter **4**, 4719 (1992)
- 25 H.-J. Reyher, N. Hausfeld, M. Pape: J. Phys.: Condens. Matter **12**, 10599 (2000)
- 26 R. Scharfschwerdt, A. Mazur, O.F. Schirmer, H. Hesse, S. Mendricks: Phys. Rev. B **54**, 15284 (1996)
- 27 C.H. Henry, C.P. Slichter: in *Physics of Color Centers*, ed. by W.B. Fowler (Academic, New York 1968) p.378
- 28 A.J. Wojtewicz, M. Kazmierczak, A. Lempicki, R.H. Bartram: J. Opt. Soc. Am. B **6**, 1106 (1989)
- 29 J.A. Weil, J.R. Bolton, J.E. Wertz: *Electron Paramagnetic Resonance* (Wiley, New York 1994) p. 497
- 30 W.B. Fowler: in *Physics of Color Centers*, ed. by W.B. Fowler (Academic, New York 1968) p. 72
- 31 M. Kaczmarek, R.W. Eason, I. Mnushkina: Appl. Phys. B **68**, 813 (1999)
- 32 Institut Fresenius, 65 232 Taunusstein, Germany
- 33 Mikroanalytisches Labor Pascher, 53 424 Remagen, Germany
- 34 N.V. Kukhtarev, V.B. Markov, S.G. Odoulov, M.S. Soskin, V.L. Vinetski: Ferroelectrics **22**, 949 (1979)
- 35 P. Delaye: private communication (2003)
- 36 F.P. Strohkendl, J.M.C. Jonathan, R.W. Hellwarth: Opt. Lett. **11**, 312 (1986)
- 37 M.B. Klein: in *Topics in Applied Physics: Photorefractive Materials and Their Applications I*, ed. by P. Günter, J.-P. Huignard (Springer, Berlin, Heidelberg 1988) p.213
- 38 X.W. Zhang, Y.H. Han, M. Lal, D.M. Smyth: J. Am. Ceram. Soc. **70**, 100 (1987)
- 39 T. Woike: private communication (2003)
- 40 T. Varnhorst, O.F. Schirmer, H. Kröse, R. Scharfschwerdt, T.W. Kool: Phys. Rev. B **53**, 116 (1996)
- 41 S. Lenjer, O.F. Schirmer, H. Hesse, T.W. Kool: Phys. Rev. B **66**, 165106 (2002)
- 42 O.F. Schirmer, H.-J. Reyher, M. Wöhlecke: in *Insulating Materials for Optoelectronics*, ed. by F. Agulló-López (World Scientific, Singapore 1995)
- 43 R.D. Shannon, C.T. Prewitt: Acta Crystallogr. B **25**, 925 (1969)
- 44 W. Kleemann, H. Schremmer: Phys. Rev. B **40**, 7428 (1989)
- 45 G. Malovichko, V. Grachev, R. Pankrath, O. Schirmer: Ferroelectrics **258**, 169 (2001)
- 46 H. Veenhuis, T. Börger, K. Buse, C. Kuper, H. Hesse, E. Krätzig: J. Appl. Phys. **88**, 1042 (2000)
- 47 O.F. Schirmer, W. Berlinger, K.A. Müller: Solid State Commun. **16**, 1289 (1975)
- 48 C. Mingjun, S.X. Dou, Z. Yong, Y. Peixian: Opt. Commun. **170**, 115 (1999)
- 49 G. Roosen, S. Bernhardt, P. Delaye: Opt. Mater. **23**, 243 (2002)
- 50 K.H. Hellwege, A.M. Hellwege (eds.): *Landolt-Börnstein III, Numerical Data and Functions in Science and Technology, Vol. 16a* (Springer, Berlin, Heidelberg 1981)
- 51 K. Buse, S. Riehemann, S. Loheide, H. Hesse, F. Mersch, E. Krätzig: Phys. Status Solidi A **135**, K87 (1993)
- 52 M. Simon, F. Mersch, C. Kuper, S. Mendricks, S. Wevering, J. Imbrock, E. Krätzig: Phys. Status Solidi A **159**, 559 (1997)
- 53 W.J. Merz: Phys. Rev. **76**, 1221 (1949)
- 54 C. Veber: Diploma thesis, University of Osnabrück (1998)
- 55 U. van Stevendaal: PhD thesis, University of Osnabrück (1998)